

Article

A Novel Design to Eliminate Lüders Band in Medium-Mn Steel and Its Microstructure-Property Relationship

Rendong Liu ^{1,2}, Zhiping Hu ^{1,2,*}, Chunqing Lin ^{1,2,*}, Dapeng Yang ³, Xingli Gu ^{1,2}, Xin Xu ^{1,2} and Jinyu Guo ^{1,2}

¹ State Key Laboratory of Metal Material for Marine Equipment and Application, 63 Wuyi Road, Anshan 114009, China; ag_lrd@126.com (R.L.); gu_xingli@126.com (X.G.); ag_xuxin@163.com (X.X.); jyguo9@163.com (J.G.)

² Technology Center of Angang Steel Company Limited, 63 Wuyi Road, Anshan 114009, China

³ The State Key Laboratory of Rolling and Automation, Northeastern University, Shenyang 110819, China; yangdapeng@ral.neu.edu.cn

* Correspondence: huzhiping900401@126.com (Z.H.); linchunqing1@126.com (C.L.);
Tel.: +86-04126721025 (Z.H. & C.L.)

Abstract: In the current work, we design a novel medium Mn steel with a superior mechanical property and no Lüders band. For industrial applications, a “low Mn addition” chemical composition and two kinds of different annealing processes with various initial microstructures were introduced. Consequently, the sample subjected to full austenitized quenching plus intercritical annealing process exhibited an outstanding mechanical property without the Lüders band. The microstructural evolution and austenite reverted transformation behavior were discussed in detail. In addition, austenite stability was estimated by chemistry stability and mechanical stabilization. It seemed that the austenite stability was significantly influenced by the morphological component. Thus, the sample with single lath-like ferrite and austenite exhibited the most excellent mechanical property. Furthermore, the “Lüders band” phenomenon was considered to rely on the restriction of martensitic recovery and recrystallization by lath-like morphology. The occurrence of the Lüders band was attributed to the low work-hardening ability caused by dynamic recovery. The formation of lath-like morphology could prevent the occurrence and propagation of the Lüders band by increasing the dislocation density and active TRIP effect.

Keywords: medium Mn steel; mechanical property; Lüders band; morphology; initial microstructure; TRIP effect; work-hardening



Citation: Liu, R.; Hu, Z.; Lin, C.; Yang, D.; Gu, X.; Xu, X.; Guo, J. A Novel Design to Eliminate Lüders Band in Medium-Mn Steel and Its Microstructure-Property Relationship. *Crystals* **2023**, *13*, 936. <https://doi.org/10.3390/cryst13060936>

Academic Editor: Umberto Prisco

Received: 17 May 2023

Revised: 5 June 2023

Accepted: 7 June 2023

Published: 10 June 2023



Copyright: © 2023 by the authors. Licensee MDPI, Basel, Switzerland. This article is an open access article distributed under the terms and conditions of the Creative Commons Attribution (CC BY) license (<https://creativecommons.org/licenses/by/4.0/>).

1. Introduction

Currently, reducing CO₂ emissions is significant for the environment and energy-saving. For the automotive industry, lighting weight and improving crash safety are necessary. Thus, increasing the application of advanced high-strength steels (AHSSs) with a good combination of strength and formability is crucial. Among various AHSSs, medium Mn steel with Mn addition between 3 and 10 wt.% is considered ideal to meet the requirements mentioned above [1–7]. The medium-Mn steel concept was first proposed by Miller [8] due to the considerable mechanical property of 6Mn steel. Subsequently, M. J. Merwin reported a low-carbon Mn TRIP steel using an intercritical annealing process known as austenite reverse transformation (ART) [9]. Since then, research on medium Mn steel has concentrated on various alloying systems and annealing processes [10–13]. Targeted microstructures comprising ferrite and retained austenite (20–40 vol.%) is a feature shared by all of the diversified research [11,12,14–16]. During deformation, retained austenite undergoes martensitic transformation by the transformation-induced plasticity (TRIP) effect, contributing to a prominent increase in strength and ductility [14,15]. As a result, many studies exhibited an ideal combination of the ultimate tensile strength

(UTS) of 800–1300 MPa and TE of 25–60% by optimizing alloying design, adjusting ART temperatures, and ART time [10,13,16].

However, there is no commercial medium-Mn production method to apply to automotive parts due to a series of industrial problems. High alloying elements addition (C and Mn) contributed to high hardenability, resulting in a full martensitic matrix after cooling to room temperature (RT), which is difficult to cold work. In addition, the annealing temperatures for ART are within the limits of the continuous annealing line, as reported in earlier research [11,13,14]. The annealing time for ART is also unsuitable for a limited industrial continuous time due to a long Mn diffusing period for austenite [17,18]. Furthermore, the nature of the severe Lüders band was observed with cold-rolled medium-Mn steel, leading to a poor surface for stamped parts. Many studies focused on these problems and offered solutions [19–21]. Al was added to increase the Ac₃, contributing to a higher annealing temperature suitable for continuous annealing [22,23]. In addition, a Si-Al system was designed in 6–10 Mn steels to adjust the stacking fault energy (SFE) ranging from 18 to 25 J/cm², resulting in a different strain hardening behavior of TRIP and TWIP (twinning induced plasticity) for high mechanical properties [24,25]. This approach benefited Mn-enrichment in austenite due to an initial high Mn content.

A serious Lüders band issue also exploited the application of medium Mn steel. The studies on the formation and propagation of the Lüders band were frequently reported [26–28], and many techniques to eliminate the Lüders band were developed, including low carbon addition [29], the initial microstructure of martensite [29,30], and pre-deformation addition [31]. Industrial manufacturing requires a cold-rolled medium Mn steel with high Mn enrichment in austenite and free Lüders band.

In the present work, a novel chemical composition for industrial medium Mn steel was designed with “a low Mn addition” alloying concept. Different annealing processes were applied to achieve the high mechanical property combination. Three different annealing processes with three types of initial microstructures were applied to the designed medium Mn steel. The microstructural evolution and the relationship between the microstructure and mechanical properties were systematically investigated. The effects of austenite stability and the behavior of austenite reversed transformation were discussed. Influencing factors of the Lüders band were also analyzed.

2. Materials and Methods

The chemical composition of the experimental steel is listed in Table 1. The steel was cast as a 135 kg ingot in a vacuum induction furnace and then hot forged into a slab with a cross-section dimension of 80 mm × 80 mm. The steel was isothermally solution-treated at 1250 °C for 2 h and then rough hot rolled to a 35 mm-thick slab. Subsequently, a 35 mm-thick slab was reheated to 1250 °C and held at 1200 °C, and then hot-rolled to a 2.8 mm-thick plate via 7 passes with a reduction of 30%, and the finish rolling temperature was 910 °C. The hot-rolled plate was retarded and cooled to room temperature from 650 °C, simulating the coiling process. Afterward, the as-hot-rolled plate was cold-rolled to 1.6 mm. The Ac₁ and Ac₃ temperature of the cold-rolled steel was detected by a quench dilatometer (DIL 805A), in which the heating rates were 1 °C s⁻¹, and the cooling rates were 0.5, 1, 5, 10, and 20 °C s⁻¹. The result is shown in Figure 1a. A_{c1} and A_{c3} temperatures of the cold-rolled sample were 672 °C and 908 °C, respectively. In addition, only martensitic transformation is observed due to the high hardenability, as shown in Figure 1b. After the cold-rolling, the plates were subjected to three different annealing processes, as shown in Figure 2. The 1# annealing process was single intercritical annealing at different temperatures for 10 min, which were named the IA-700, IA-730, IA-760, and IA-790 samples. The 2# annealing process was intercritical quenching (810 °C) or full austenitization quenching (910 °C) for 5 min, followed by a second intercritical annealing (730 °C) for 5 min, and the samples were named Q810-IA730 and Q910-IA730, respectively.

Table 1. The chemical composition of the tested steel (wt.%).

C	Mn	Si	Al	V	Fe
0.25	3.4	0.5	1.5	0.1	Bal.

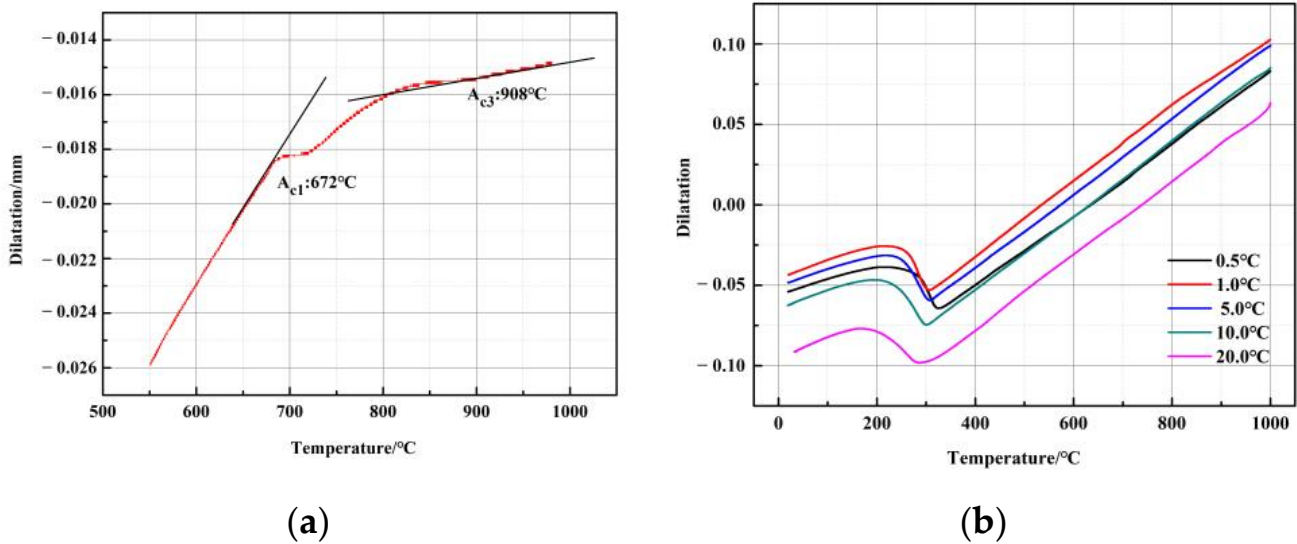


Figure 1. Dilatometric results of cold-rolled steel during the heat treatments (a) A_{c1} and A_{c3} temperature of cold-rolled steel measured during the heating process; (b) dilatometric results of the steel during the cooling process.

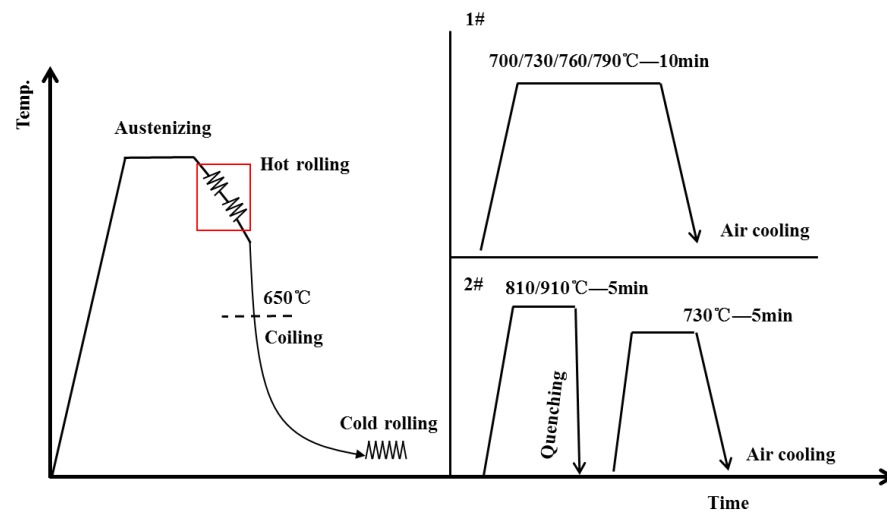


Figure 2. Schematic diagram of the rolling process and heat treatments for the medium-Mn steel.

The microstructural morphology was characterized using scanning electron microscopy (SEM). The samples for SEM were grounded and mechanically polished, then etched with 4% nital for 20 s. Transmission electron microscopy (TEM) studies were carried out using a TECNAI G220 microscope at an operating voltage of 200 kV. The sample with a thickness of $40\mu\text{m}$ was electro-polished at -20°C in a twin-jet machine for TEM observation.

The volume fraction of retained austenite was measured by a D/max2400 X-ray diffractometer (operated at 56 kV, 182 mA) with Cu $K\alpha$ radiation at room temperature. During the experiment, a 2θ range from 40° to 120° was step-scanned with a scanning speed of $2^{\circ}/\text{min}$. The X-ray diffraction (XRD) measurements specimens were mechanically grounded and electro-polished to minimize the possible error originating from the mechanically induced transformation of the retained austenite during the sample preparation. The XRD sample

was located in the gauge of the tensile sample. Integrated intensities of the (200) α and (211) α peaks, as well as (200) γ , (220) γ , and (311) γ peaks, were used to estimate the austenite content. The volume fraction of the austenite V_γ was calculated using the following equation [21]:

$$V_\gamma = 1.4I_\gamma / (I_\alpha + 1.4I_\gamma), \quad (1)$$

where I_γ is the integrated intensity of austenite, and I_α is the integrated intensity of α -phase. Tensile test samples with a width of 6 mm and length of 25 mm were machined with their axis oriented parallel to the rolling direction. The tensile test was conducted using a CMT5105-SANS machine at room temperature with a draw speed of 2 mm/min. Three samples for each condition were tested, and the average values were calculated.

3. Results

3.1. Microstructure and Mechanical Properties of 1# Annealing Process

Figure 3a–d shows the SEM morphology of the samples that underwent the 1# annealing process. As seen in Figure 3a, a large volume of cementite was distributed in the ferrite grains, and few austenite grains could be observed, which indicated that it was difficult for cementite to dissolve and for austenite grains to nucleate under a relatively low annealing temperature in the 1#IA700 samples. Figure 3b shows that the 1#IA730 sample had a significant proportion of austenite and no obvious cementite. This indicated that the increasing temperature accelerated cementite's dissolving, contributing to austenite reverted transformation. As shown in Figure 3c,d, the austenite fraction gradually reduced as the annealing temperature increased to 760 °C and 790 °C, while the martensite fraction increased, contributing to austenite's lower thermal stability.

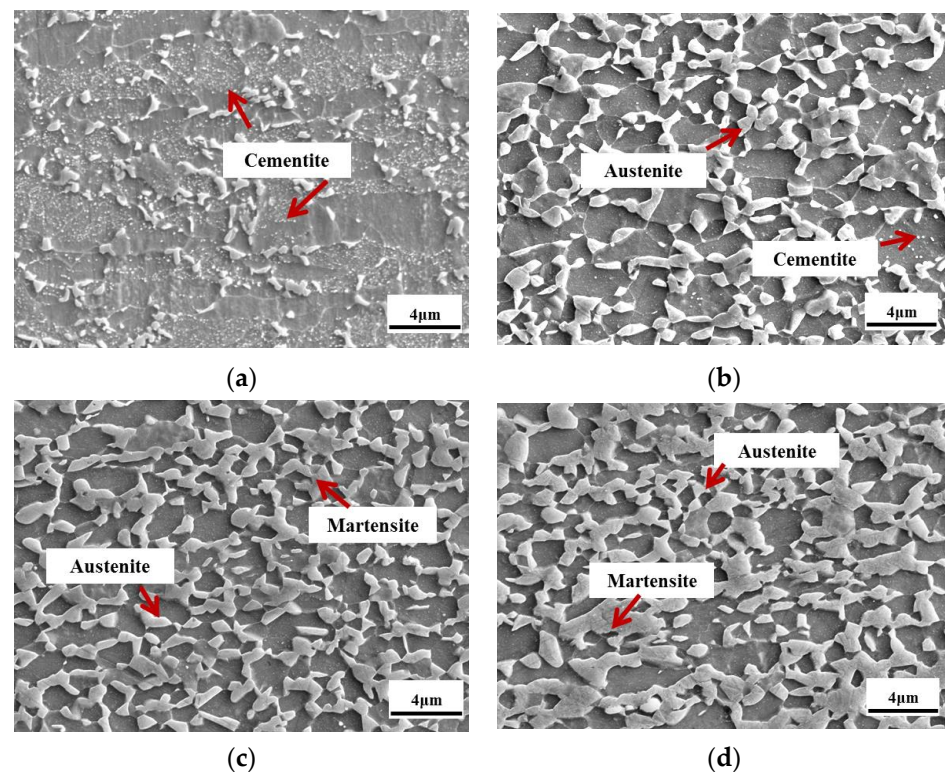


Figure 3. SEM morphology of the samples that underwent a 1# annealing process. (a) 1#IA700, (b) 1#IA730, (c) 1#IA760, and (d) 1#IA790.

Figure 4a represents the engineering stress and strain curves of the 1# annealing process. The yield strength, tensile strength, and total elongation of the 1#IA700, 1#IA730, 1#IA760, and 1#IA790 samples are listed in Table 2. Figure 4b demonstrates the yield point elongation (YPE) of the 1# annealing process, with continuous yield in the 1#IA790 sample

and values of 5.21%, 4.51%, and 3.66% for the 1#IA700, 1#IA730, and 1#IA760 samples, respectively. Figure 4c shows the austenite volume fraction of the 1# annealing process using XRD analysis. The volume fraction of austenite in the 1#IA700, 1#IA730, 1#IA760, and 1#IA790 samples was 15.6%, 20.5%, 12.8% and 6.4%, respectively. The product of strength and elongation (PSE) of samples from the 1# annealing process is displayed in Figure 4d, namely, 16,594.5 MPa·% in 1#IA700, 32,701.6 MPa·% in 1#IA730, 11,823 MPa·% in 1#IA760, and 6938.4 MPa·% in 1#IA790. Obviously, the 1#IA700 sample exhibits poor tensile strength due to the ferrite matrix and limited austenite fraction. The 1#IA760 and 1#IA790 samples have high tensile strength due to the high martensite content. The 1#IA730 sample possesses well-balanced strength and elongation performance, contributing to the optimizing microstructure and a relatively high austenite fraction.

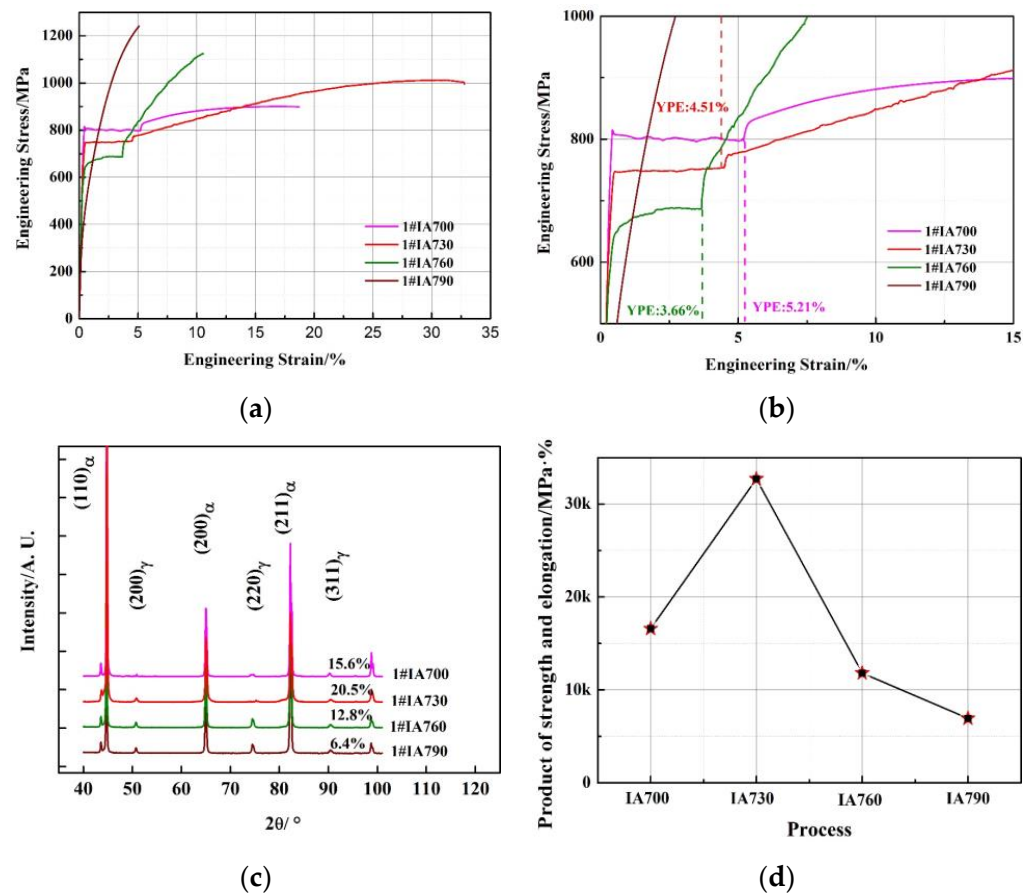


Figure 4. (a) Engineering stress-strain curves of the 1# annealing process, (b) YPE of the 1# annealing process, (c) austenite volume fraction of the 1# annealing process, and (d) PSE of the 1# annealing process.

Table 2. Mechanical properties of samples with the 1# annealing process.

Sample	Yield Strength/MPa	Tensile Strength/MPa	Total Elongation/%
1#IA700	805	897	18.5
1#IA730	734	997	32.8
1#IA760	652	1126	10.5
1#IA790	408	1239	5.6

3.2. Microstructure and Mechanical Properties of 2# Annealing Process

Figure 5a–d describes the SEM microstructure of the samples that underwent a 2# annealing process. In Figure 5a, the microstructure is mainly composed of ferrite, martensite, and a limited amount of austenite which was retained due to the small grain size and

relatively high stability [32]. Figure 5b exhibits the microstructure of ferrite and austenite. In addition, it is evident that two types of austenite and ferrite morphology were formed, namely, lath-like and block-like. It can be inferred that the block-like austenite and ferrite grains resulted from the retained block-like austenite and ferrite grains in the 2#Q810 sample, and the lath-like austenite and ferrite grains contributed to the ART on the martensitic matrix of the 2#Q810 sample. A 910 °C quenching process was applied to obtain a full martensitic morphology, as shown in Figure 5c. Obviously, after 910 °C annealing, the steel was fully austenitized, in accordance with the Ac3 (908 °C) detected in Figure 2. Figure 5d shows the microstructural morphology of the 2#Q910-IA730 sample. A dual phase consisting of lath-like austenite and ferrite distributed, contributing to the ART on the full martensitic matrix of the 2#Q910 sample.

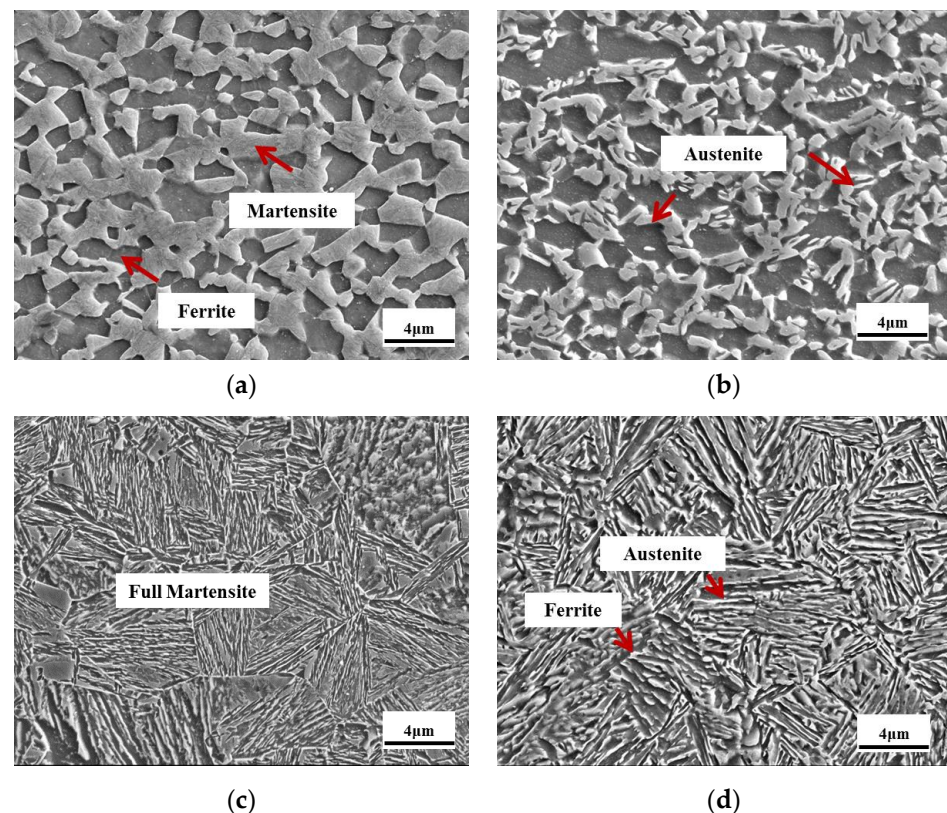


Figure 5. SEM morphology of the samples that underwent a 2# annealing process. (a) 2# Q810, (b) 2#Q810-IA730, (c) 2#Q910, and (d) 2#Q910-IA730.

Figure 6a describes the engineering stress and strain curves of the 2# annealing process. The mechanical properties of the 2#Q810-IA730 and 2#Q910-IA730 samples are listed in Table 3. Figure 6b shows the YPE of the 2# annealing process. Compared to the 1#IA730 sample, it is clear that the YPE of the 2#Q810-IA730 reduced to 3.04%, and additionally, the YPE of the 2#Q910-IA730 sample exhibited continuous yield behavior. Figure 6c represents the austenite volume fraction of the 2# annealing process by XRD analysis. The austenite volume fractions of the 2#Q810-IA730 and 2#Q910-IA730 samples were 25.4% and 28.9%, respectively. PSE of the 2# annealing process is shown in Figure 6d, with 40,504 Mpa·% for the 2#Q810-IA730 sample and 49,650 MPa·% for the 2#Q910-IA730 sample. Interestingly, after intercritical or full-austenitization quenching pre-treatment, the YPE reduced, the austenite fraction increased, and the comprehensive mechanical property enhanced.

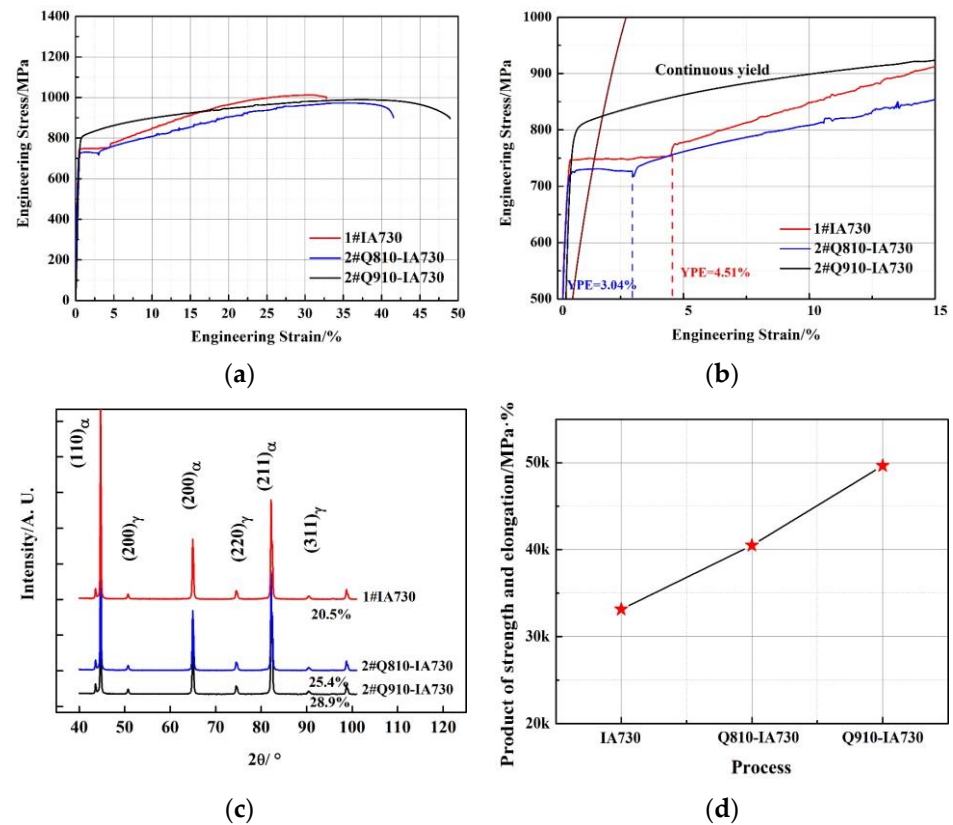


Figure 6. (a) Engineering stress-strain curves of the 2# annealing process, (b) YPE of the 2# annealing process, (c) austenite volume fraction of the 2# annealing process, and (d) PSE of the 2# annealing process.

Table 3. Mechanical properties of samples with the 2# annealing process.

Sample	Yield Strength/MPa	Tensile Strength/MPa	Total Elongation/%
2#Q810-IA730	727	973	41.5
2#Q910-IA730	811	998	49.5

4. Discussion

4.1. Austenite Reverse Transformation Behavior

According to the observations in Figures 3 and 5, it is apparent that different austenite morphologies were obtained after different annealing processes. TEM observation was used to analyze the austenite evolution in detail, as shown in Figure 7. Figure 7a describes the TEM morphology of the 1#IA730 sample and the corresponding diffraction spot. Obviously, the austenite in the 1#IA730 sample displayed a block-like morphology and was distributed on the recrystallized ferrite grain boundaries. As mentioned above, 1#IA730 was the optimal annealing process due to the relatively high austenite fraction and good strength-ductility combination. Under the low temperature in the 1#IA700 sample, not enough austenite formed; instead, cementite was distributed dispersedly. When samples 1#IA760 and 1#IA790 were exposed to a high temperature, the martensite fraction gradually increased due to the decreasing austenite thermal stability [33]. Thus, it was obvious that during the 1# annealing process, the degree of C and Mn enrichment was crucial to the austenite reversed transformation and that ferrite recrystallization proceeded effectively due to the sufficient strain stored energy. At lower annealing temperatures, it was difficult to dissolve cementite, hindering the proceeding of austenite reversed transformation. At higher temperatures, low average C and Mn content are distributed in a high amount of austenite, leading to low phase stability and martensitic transformation during cooling. Figure 7b shows the TEM morphology and associated diffraction spot of the 2#Q810

sample. Austenite grain was observed with a small grain size of about ~ 700 nm, while martensite grain appeared with a high grain size of about ~ 1000 nm. Figures 3 and 5 show that 810°C was a relatively high intercritical annealing temperature, resulting in a high austenite fraction and low stability during cooling. Accordingly, the majority of austenite grains in the intercritical region transformed to martensite after quenching, and only a small part of austenite with a small grain size was retained due to the relatively high stability [34]. Figure 7c presents the TEM morphology and the corresponding diffraction spot of the 2#Q810-IA730 sample. Clearly, two types of austenite are exhibited in the microstructure, namely, block-like and lath-like. The block-like austenite grains were the small ones retained in the 2#Q810 sample. The lath-like austenite was transformed from the martensite of the 2#Q810 sample, which proved the occurrence of the second austenite reversed transformation on the martensitic matrix. Figure 7d shows the TEM morphology and the corresponding diffraction spot of the 2#Q910-IA730 sample. Lath-like austenite and ferrite are distributed on the whole microstructure. This indicates that sufficient austenite reversed transformation occurred on the full martensitic matrix obtained in the 2#Q910 sample.

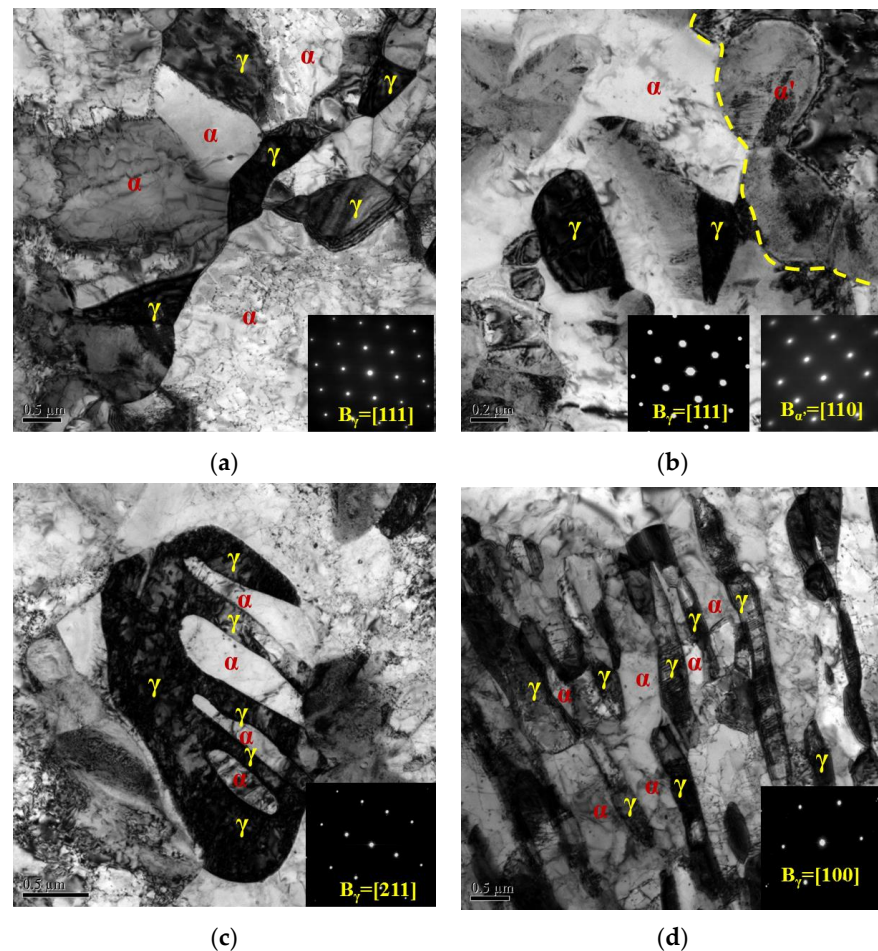


Figure 7. TEM morphology and the corresponding diffraction spot of different samples. (a) 1#IA730, (b) 2#Q810, (c) 2#Q810-IA730, and (d) 2#Q910-IA730.

Figure 8 demonstrates the orientation maps of austenite and the microstructure of the sample under different processes, respectively. As shown in Figure 8a,b, it was obvious that the austenite grains exhibited random orientations. This indicates that cold-rolling deformation broke the martensitic structure of the hot-rolled sample. As a result, during the subsequent intercritical annealing, the austenite grains nucleated and grew randomly oriented from the martensite with C and Mn enrichment. In addition, ferrite recovery and recrystallization proceeded to release the strain energy [35]. Consequently, ferrite exhibited

as block-like and austenite distributed on the ferrite grain boundaries as a block-like type (Figure 7a). In contrast, it can be seen in Figure 8c,d that the austenite grains in some packets have the same orientation. This demonstrates that austenite inherited the morphology of quenched martensite, and only nucleation and growth proceeded effectively. The recrystallization of the untransformed martensite was restricted by surrounding lath-like austenite, and the martensite recovered to ferrite by the reduction of dislocations accompanied by the partition of C to austenite so that ferrite exhibited lath-like morphology and crystallographic orientation of quenched martensite. In summary, deformed martensite provided sufficient stored strain energy, leading to a high degree of martensitic recovery and recrystallization, resulting in block-like morphology and random orientation. However, not enough strain energy could be obtained only by quenching, leading to the restriction of martensitic recovery and recrystallization, contributing to retaining the lath-like morphology and the same orientation.

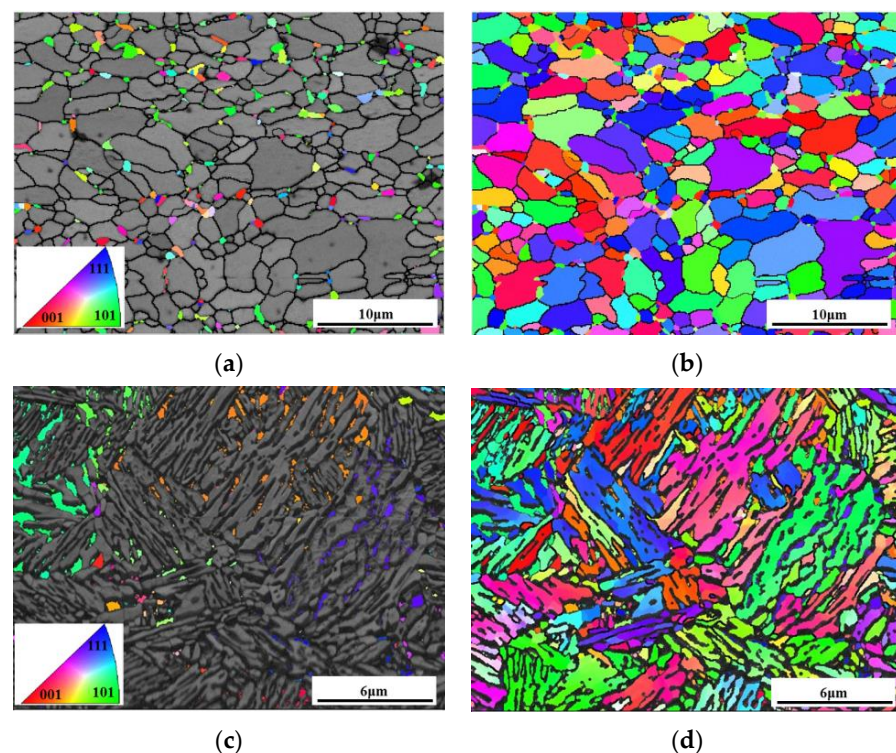


Figure 8. EBSD analysis of different samples. (a,b) orientation maps of austenite and microstructure of the 1#IA730 sample, (c,d) orientation maps of austenite and microstructure of the 2#Q910-IA730 sample.

4.2. Austenite Stability and Work-Hardening Behavior

Controlling the austenite fraction and stability is necessary to achieve a positive mechanical strength and ductility combination in medium Mn steel [10]. Three critical factors influence the stability of the metastable austenite at room temperature: chemistry stability, grain size, and mechanical stability. For chemistry stability, both C and Mn are strong austenite stabilizers. Especially in medium Mn steel, the addition of Mn can result in a stable austenite equilibrium at room temperature [14]. For grain size, a small grain size affects the austenite stability by lowering the martensite start temperature [29]. For mechanical stabilization, the correct amount of dislocations in austenite effectively suppresses the transformation kinetics of martensite [36]. Figure 9a–c represents the detected points in the microstructure of the 1#IA-730, 2#Q810-IA730, and 2#Q910-IA730 samples. Mn concentration of different annealed samples using SEM-EDS analysis is exhibited in Figure 9d. Among the three different annealed samples, the Mn content in the austenite grains of the 2#Q810-IA730 sample and 1#IA730 sample was obviously the highest and the lowest. In the 1# process, the optimizing annealing window was

narrow. As Figure 3 shows, at a lower annealing temperature (700 °C), a large amount of cementite did not dissolve, while at a higher annealing temperature (760 °C), a significant amount of martensite formed. Consequently, 730 °C was a relatively suitable annealing temperature for the 1# process. However, 730 °C was relatively low for Mn effective partitioning. In addition, it was shown in Figure 3 that some cementite was also distributed on the matrix of 1#IA730, and the formation of cementite on ferrite occupied a certain amount of Mn atoms, which decreased the Mn concentration in austenite. In the 2#Q810 process, Mn diffusion was promoted, and a relatively high Mn enrichment was retained in martensite after quenching. In the 2#Q810-IA730 sample, a higher Mn enrichment is obtained in austenite grains. Mn enrichment in block-like austenite contributed to the sustaining Mn partitioning from the neighboring block-like ferrite during the second IA process. Mn enrichment in lath-like austenite was associated with the higher initial Mn enrichment in the 2#Q810 sample martensite and the nanoscale lath width, which shortened the distance of Mn diffusion. Additionally, the 2#Q910-IA730 sample exhibited a higher Mn enrichment than the 1#IA730 sample and a lower Mn enrichment than the 2#Q810-IA730 sample. Compared to the 2#Q810-IA730 sample, no initial Mn partitioning from ferrite to austenite proceeded in the 2#Q910-IA730 sample due to the full austenitizing quenching temperature. Interestingly, the 2#Q910-IA730 sample had a higher Mn enrichment than the 1#IA730 sample, even though there had been no initial Mn partitioning from ferrite to austenite in either sample. This result was considered to rely on two main reasons. Firstly, the undissolved cementite in the 1#IA730 sample occupied some amount of Mn content; however, in the 2#Q910-IA730 sample, the 910 °C quenching temperature was high enough for cementite to dissolve. Secondly, the lath-like structure promoted Mn partitioning similar to 2#Q810-IA730 mentioned above. Thus, it could be sure that the initial quenching and second intercritical annealing process benefited Mn partitioning and enhanced austenite chemistry stability by constructing the lath-like morphology.

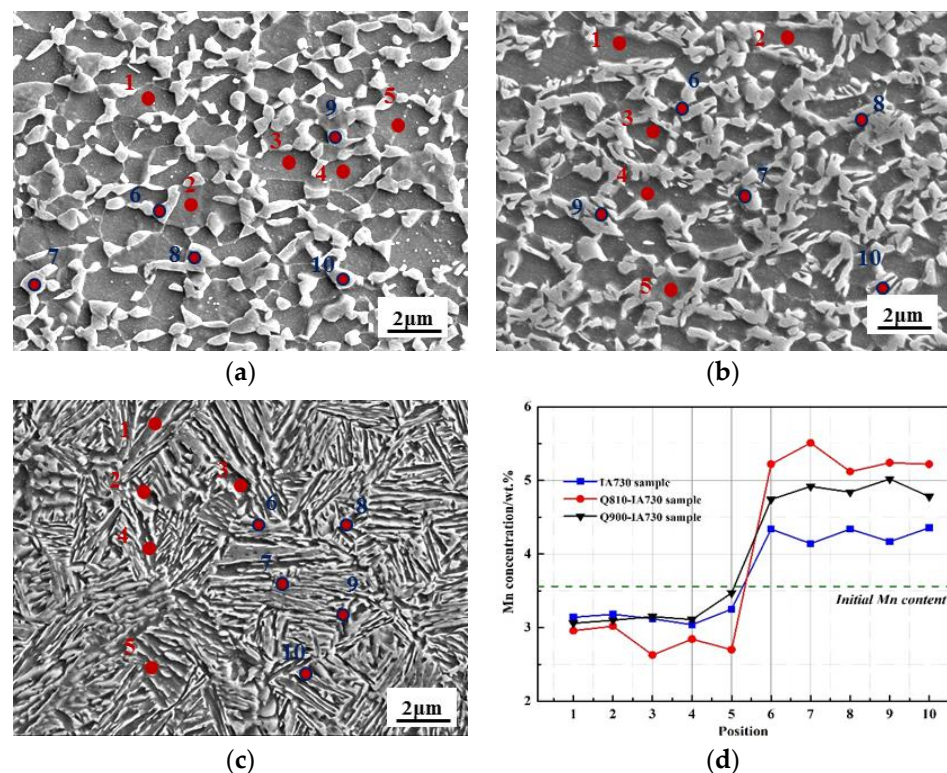


Figure 9. SEM morphology of the (a) 1#IA-730 sample, (b) 2#Q810-IA730 sample, and (c) 2#Q910-IA730, (d) Mn concentration of different annealed samples using SEM-EDS analysis according to the points marked in (a–c). 1 to 5 detected points were in ferrite, and 6 to 10 detected points were in austenite in the corresponding microstructure.

The work-hardening (WH) curves were introduced to estimate austenite mechanical stability, as shown in Figure 10a. A1, B1, and C1 are the first obvious inflection points of the 1#IA730, 2#Q810-IA730, and 2#Q910-IA730 samples in the WH curves, respectively. As D.K. Wilsdorf reported, the reduction of WH at an early stage was considered a dynamic recovery of dislocations of ferrite [22]. It was shown that three WH curves exhibited an apparent reducing trend at the early stage. On the other hand, whereas the corresponding WH rates of A1 and B1 were near 740 MPa, the corresponding WH rate of C1 was close to 2745 MPa. Clearly, C1 was much higher than A1 and B1. This result contributed to the different ferrite morphologies. In both 1#IA730 and 2#Q810-IA730 samples, a large amount of block-like ferrite grains formed during intercritical annealing. As mentioned above, the acquirement of block-like ferrite relied on sufficient recovery and recrystallization, leading to a low density of dislocations in ferrite. Thus, compared to the neighboring austenite grains, block-like ferrite exhibited lower strength and deformed preferentially during tensile deformation. However, ferrite exhibited a lath-like morphology in the 2#Q910-IA730 sample due to inactive recovery and recrystallization. Due to the retention of a relatively high density of dislocations, the lath-like ferrite had a relatively high strength comparable to the neighboring austenite grains. Thus, ferrite and austenite grains deformed together during the tensile deformation. Then, austenite underwent the TRIP effect to transform into martensite, leading to a slow dropping after C1. A2, B2, and C2 were the inflection points of sharp increase of 1#IA730, 2#Q810-IA730, and 2#Q910-IA730 samples in WH curves, respectively. As Cai reported, the sharp increase was associated with the active TRIP effect of austenite grain in medium Mn steel [24]. It was demonstrated that the corresponding strain of A2 was the lowest, and the corresponding strain of B2 was lower than C2. This contributed to the austenite stability. It was shown that the austenite grains exhibited low chemistry stability due to the low Mn enrichment and block-like morphology in the 1#IA730 sample. The cooperation led to the occurrence of an active TRIP effect. Interestingly, the austenite grains in the 2#Q810-IA730 sample exhibited higher chemistry stability than in the 2#910-IA730 sample; however, the corresponding strain of C2 was higher than B2. This was associated with the preferential TRIP effect of block-like austenite in the 2#Q810-IA730 sample. To prove the occurrence of TRIP at different strains, Figure 10b was introduced. In the 1#IA730 sample, the curve of the austenite fraction at different strains was divided into two stages (S1 and S2). During S1, a small dropping of austenite fraction appeared due to dynamic recovery, and during S2, a sharp dropping of austenite fraction appeared due to the active TRIP effect, which matched agreement with our previous discussion. In the 2#Q810-IA730 sample, the curve of austenite fraction at different strains was divided into three stages (S1, S2, and S3). The S1 in the 2#Q810-IA730 sample was similar to the 1#IA730 sample. S2 showed a sharp dropping trend associated with the TRIP effect of block-like austenite. S3 presents a relatively gradual decreasing trend due to the sustain TRIP effect of the rest lath-like austenite. Differently in the 2#Q910-IA730 sample, the curve of austenite fraction at different strains was divided into three stages (S1, S2, and S3). However, during S1, an obvious reduction of austenite content was observed. This result is consistent with the slow-dropping trend shown in Figure 10a; the TRIP effect proceeded at an early stage due to the similar strength of lath-like ferrite and austenite. Compared to the S2 in the 2#Q810-IA730 sample, the S2 in the 2#Q910-IA730 sample showed a slower dropping trend. This indicates that lath-like austenite exhibited higher stability than block-like austenite. Then, S3 in the 2#Q910-IA730 sample presented a similar dropping trend to the 2#Q810-IA730 sample.

In addition, the relationship between the austenite volume fraction f_γ and true strain ϵ of the three annealed samples was estimated by the exponent formula [36]:

$$f_\gamma = f_0 \cdot \exp(-k\epsilon), \quad (2)$$

where f_0 is the austenite volume fraction before tensile deformation, k is constant, which reflects the mechanical stability of austenite, and a lower k value means higher mechanical stability of austenite. The k values of the 1#IA730, 2#Q810-IA730, and 2#Q910-IA730

samples were 7.37, 6.51, and 6.48, respectively. Obviously, the 1#IA730 sample exhibited the lowest mechanical stability among the three annealed processes due to low chemistry stability and block-like morphology. The 2#Q810-IA730 sample exhibited similar austenite stability to the 2#Q910-IA730 sample. This could be inferred that the factor of morphology plays a more significant role than the factor of chemical stability.

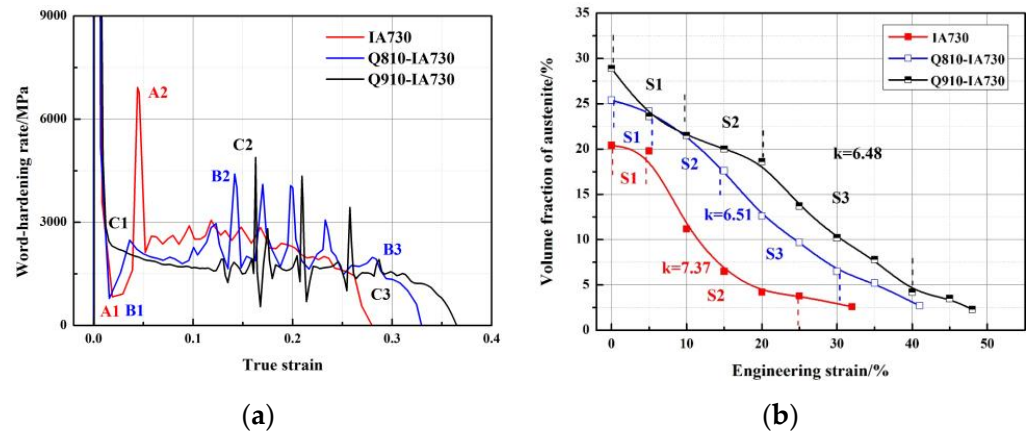


Figure 10. (a) Work-hardening curves and (b) austenite fraction at different engineering strains of different annealed samples.

4.3. The Influence Factors of Lüders Band

Figure 11 shows the yield point elongation (YPE) of different annealed samples subjected to the 1# and 2# processes. In the 1# process, it was shown that the YPE reduced with the increasing annealing temperature. This result was obtained in numerous reports [25,28,29,36]. As Luo et al. reported in the medium-Mn steels with a composition of Fe-5Mn-0.1/0.2 C, the change of YPE was considered to associate with the solute C atoms in ferrite [29]. However, a similar result was obtained in K. Steineder et al. [27] work under the given condition of a similar temperature range and long annealing time. Therefore, they argued that C partitioning should not be restricted and the YPE was related to austenite stability at RT. This was in agreement with our result. High intercritical annealing temperature resulted in a high amount of intercritically formed austenite; however, low stability at RT. Indeed, the Lüders band contributed to the low WH ability caused by dynamic recovery, as shown in Figures 4a and 10a, leading to the localized deformation. Thus, introducing new mobile dislocations could effectively prevent the occurrence of the Lüders band. In the 1# process, high intercritical annealing temperature resulted in high intercritically formed austenite but with low RT stability. The low-stability austenite underwent the TRIP effect to provide a significant number of new mobile dislocations, enhancing the WH and eliminating the Lüders band. However, the mechanical property was weakened, as shown in Figure 4a. Hence, it was necessary to obtain excellent mechanical properties while also getting rid of the Lüders band. In the 2# process, the YPE was clearly shortened; even in the 2#Q910-IA730 sample, the YPE value was 0. This result contributed to the formation of lath-like austenite and ferrite. Figure 9 shows that the austenite grains in the 2#Q910-IA730 sample had higher chemistry stability than the 1# IA730 sample. The YPE of the 2#Q910-IA730 sample should be longer than the 1# IA730 sample. However, the result was obviously the opposite. This was related to the lath-like morphology. As mentioned above, the lath-like ferrite underwent inactive recovery and recrystallization, enhancing strength. During formation, lath-like ferrite and austenite deformed together, and WH rapidly increased due to the presence of a high density of dislocations by the TRIP effect. Thus, the Lüders band was prevented. Interestingly, in the 2#Q810-IA730 sample, both block-like and lath-like morphology existed; the YPE was also shorter than the 1#IA730 sample. It was considered that during formation, a low density of dislocations in block-like ferrite weakened WH, and no TRIP effect proceeded due to the

high stability of austenite, leading to the occurrence of the Lüders band. However, when the deformation happened on the lath-like ferrite and austenite, the TRIP effect of lath-like austenite proceeded, preventing the propagation of the Lüders band.

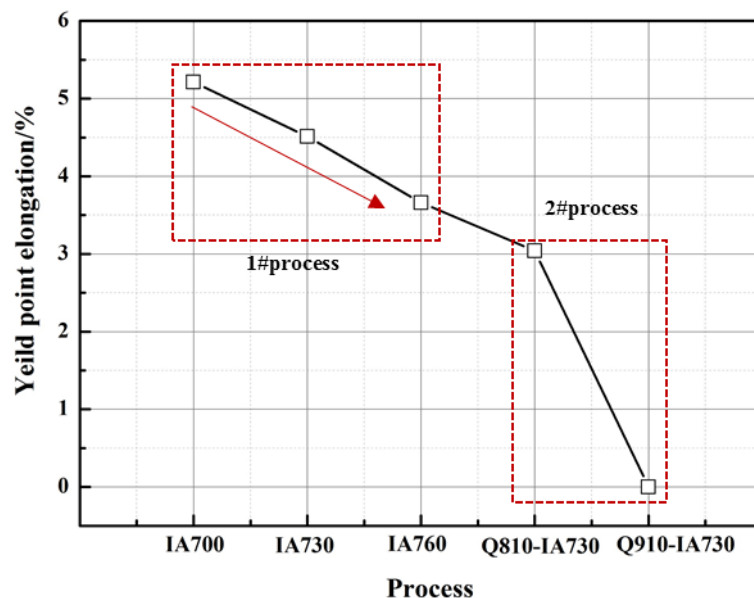


Figure 11. The yield point elongation of different annealed samples subjected to 1# and 2# process.

5. Conclusions

(1) A “low Mn addition” chemical composition and a full austenitizing quenching plus intercritical annealing process were designed for the industrial feasibility of cold-rolled medium Mn steel. A superior mechanical property of 998 MPa (TS), 49.5% (EL), and 49,650 MPa·% (PSE) was obtained in the 2#Q910-IA730 sample. It is worth mentioning that the 2#Q910-IA730 sample exhibited continuous yield behavior without the Lüders band.

(2) For the initial microstructure, deformed martensite provided sufficient stored strain energy, leading to a high degree of martensitic recovery and recrystallization, resulting in block-like morphology and random orientation. However, not enough strain energy could be obtained in the quenched martensite only by the quenching process, leading to the restriction of martensitic recovery and recrystallization, contributing to retaining lath-like morphology and the same orientation.

(3) Initial quenching and the second intercritical annealing process benefited Mn partitioning and enhanced austenite chemistry stability by constructing the lath-like morphology.

(4) Both chemistry stability and microstructural morphology determined the WH by affecting the austenite mechanical stabilization. However, the factor of morphology seemed to play a more significant role than the factor of chemical stability.

(5) By comparing the 1#IA730 sample, 2#Q810-IA730 sample, and 2#Q910-IA730 sample, it inferred that the fact of the Lüders band was mainly associated with morphology. Block-like morphology would lead to an obvious Lüders band due to the low WH ability caused by dynamic recovery. The formation of lath-like morphology could shorten and even eliminate the Lüders band by a high density of dislocations of ferrite and the contribution of the TRIP effect.

Author Contributions: Conceptualization, methodology, visualization, and writing—original draft preparation, R.L. and Z.H.; validation and writing—review and editing, C.L., D.Y. and X.G.; formal analysis, X.X.; resource, data curation, J.G. All authors have read and agreed to the published version of the manuscript.

Funding: This research was funded by the National Natural Science Foundation of Liaoning Province, China [Grant No. 2022-MS-450].

Data Availability Statement: Not applicable.

Conflicts of Interest: The authors declare no conflict of interest.

References

1. Aydin, H.; Essadiqi, E.; Jung, I.H.; Yue, S. Development of 3rd generation AHSS with medium Mn content alloying compositions. *Mater. Sci. Eng. A* **2013**, *564*, 501–508. [[CrossRef](#)]
2. Luo, H.; Shi, J.; Wang, C.; Cao, W.; Sun, X.; Dong, H. Experimental and numerical analysis on formation of stable austenite during the intercritical annealing of 5Mn steel. *Acta Mater.* **2011**, *59*, 4002–4014. [[CrossRef](#)]
3. Seo, C.; Kwon, K.; Choi, K.; Kim, K.; Kwak, K.; Lee, S.; Kim, N. Deformation behavior of ferrite–austenite duplex lightweight Fe–Mn–Al–C steel. *Scr. Mater.* **2012**, *66*, 519–522. [[CrossRef](#)]
4. Frommeyer, G.; Brux, U.; Neumann, P. Supra-Ductile and High-Strength Manganese-TRIP/ TWIP Steels for High Energy Absorption Purposes. *ISIJ Inter.* **2003**, *43*, 438–446. [[CrossRef](#)]
5. Krizan, D.; De Cooman, B.C. Mechanical properties of TRIP steel microalloyed with Ti. *Metall. Mater. Trans. A* **2014**, *45*, 3481–3492. [[CrossRef](#)]
6. Li, Z.; Xie, H.; Jia, F.; Lu, Y.; Yuan, X.; Jiao, S.; Jiang, Z. Study on Deformation Characteristics and Microstructure Evolution of 2205/AH36 Bimetal Composite in a Novel Hot Forming Process. *Metals* **2020**, *10*, 1375. [[CrossRef](#)]
7. Stradomski, G.; Rydz, D.; Garstka, T.; Pałęga, M.; Dyl, T.; Szarek, A.; Szarek, J.L.; Dembiczak, T. Influence of Asymmetric Rolling Process on the Microstructure Properties of Bimetallic Sheet Metals. *Materials* **2022**, *15*, 2013. [[CrossRef](#)]
8. Miller, R. Ultrafine-Grained Microstructures and Mechanical Properties of Alloy Steels. *Metall. Trans.* **1972**, *3*, 905–912. [[CrossRef](#)]
9. Merwin, M.J. Microstructure and Properties of Cold Rolled and Annealed Low-Carbon Manganese TRIP Steels. *Iron Steel Technol.* **2008**, *10*, 66–84.
10. Decooman, B.C.; Lee, S. Development of Medium and Intermediate Mn Third Generation Automotive Steel Grades. In Proceedings of the 2nd International Symposium on Automobile Steel, Anshan, China, 21–24 May 2013.
11. Lee, S.; Jung, Y.; Sung, K.; Kim, Y.; Kang, M.; Woo, W.; Lee, Y. The effect of nitrogen on the stacking fault energy in Fe-15Mn-2Cr-0.6C-xN twinning-induced plasticity steels. *Scr. Mater.* **2014**, *92*, 23–26. [[CrossRef](#)]
12. Cao, W.; Wang, C.; Shi, J.; Wang, M.; Hui, W.; Dong, H. Microstructure and mechanical properties of Fe-0.2C-5 steel processed by ART-annealing. *Mater. Sci. Eng. A* **2011**, *564*, 501–508. [[CrossRef](#)]
13. Luo, L.; Wei, L.; Li, W.; Shu, Z.; Jin, X. Tensile behaviors and deformation mechanism of a medium Mn-TRIP steel at different temperatures. *Mater. Sci. Eng. A* **2017**, *682*, 698–703. [[CrossRef](#)]
14. Ding, R.; Dai, Z.; Huang, M. Effect of pre-existing austenite on austenite reversion and mechanical behavior of an Fe-0.2C-8-2Al medium Mn steel. *Acta Mater.* **2018**, *147*, 59–69. [[CrossRef](#)]
15. Sun, W.; Wu, Y.; Yang, S.; Hutchinson, C. Advanced high strength steel (AHSS) development through chemical patterning of austenite. *Scr. Mater.* **2018**, *146*, 60–63. [[CrossRef](#)]
16. Avishan, B.; Garcia-Mateo, C.; Morales-Rivas, L.; Yazdani, S.; Caballero, F.G. Strengthening and mechanical stability mechanisms in nanostructures bainite. *J. Mater. Sci.* **2013**, *48*, 6121–6132. [[CrossRef](#)]
17. Arlazarov, A.; Gouné, M.; Bouaziz, O.; Hazotte, A.; Petitgand, G.; Barges, P. Evolution of microstructure and mechanical properties of medium Mn steels during double annealing. *Mater. Sci. Eng. A* **2012**, *542*, 31–39. [[CrossRef](#)]
18. Xu, Y.; Hu, Z.; Zou, Y.; Tan, X.; Han, T.; Chen, S.; Ma, D.; Misra, R. Effect of two-step intercritical annealing on microstructure and mechanical properties of hot-rolled medium manganese TRIP steel containing δ -ferrite. *Mater. Sci. Eng. A* **2017**, *688*, 40–55. [[CrossRef](#)]
19. Liang, Z.Y.; Cao, Z.H.; Lu, J.; Huang, M.X.; Tazan, C.C. Influence of co-existing medium Mn and dual phase steel microstructures on ductility and Lüders band formation. *Acta Mater.* **2021**, *221*, 117418. [[CrossRef](#)]
20. Oh, S.; Kilic, M.E.; Seol, J.; Hong, J.; Soon, A.; Lee, Y. The mechanism of dynamic strain aging for type A serrations in tensile flow curves of Fe-18Mn-0.55C (wt.%) twinning-induced plasticity steel. *Acta Mater.* **2020**, *188*, 366–375. [[CrossRef](#)]
21. Zhang, J.; Huang, M.; Sun, B.; Zhang, B.; Ding, R.; Luo, C.; Zeng, W.; Zhang, C.; Yang, Z.; van der Zwaag, S.; et al. Critical role of Lüders banding in hydrogen embrittlement susceptibility of medium Mn steels. *Scr. Mater.* **2021**, *190*, 32–37. [[CrossRef](#)]
22. Cai, Z.; Ding, H.; Misra, R.; Wu, H.; Kong, H. Unique impact of ferrite in influencing austenite stability and deformation behavior in a hot-rolled Fe–Mn–Al–C steel. *Mater. Sci. Eng. A* **2014**, *595*, 86–91. [[CrossRef](#)]
23. Li, Z.; Cai, Z.; Misra, R. The intercritical factors governing mechanical properties in hot-rolled Fe-0.2C-11Mn-(0-6)Al TRIP steels and fracture behavior. *Mater. Sci. Eng. A* **2017**, *683*, 46–55. [[CrossRef](#)]
24. Cai, Z.; Ding, H.; Xue, X.; Xin, Q. Microstructural evolution and mechanical properties of hot-rolled 11% manganese TRIP steel. *Mater. Sci. Eng. A* **2013**, *560*, 388–395. [[CrossRef](#)]
25. Lee, S.; De Cooman, B. Effect of the intercritical annealing temperature on the mechanical properties of 10 Pct Mn multi-phase steel. *Metall. Mater. Trans. A* **2014**, *45*, 5009–5016. [[CrossRef](#)]
26. Wang, X.; He, B.; Liu, C.; Jiang, C.; Huang, M. Extraordinary Lüders-strain-rate in medium Mn steels. *Materialia* **2019**, *6*, 100288. [[CrossRef](#)]
27. Steineder, K.; Krizan, D.; Schneider, R.; Béal, C.; Sommitsch, C. On the microstructural characteristics influencing the yielding behavior of ultra-fine grained medium-Mn steels. *Acta Mater.* **2017**, *139*, 39–50. [[CrossRef](#)]

28. Mahieu, J.; De Cooman, B.; Maki, J. Phase Transformation and mechanical properties of si-free CMnAl transformation-induced plasticity-aided steels. *Metall. Trans. A* **2002**, *33*, 2573–2580. [[CrossRef](#)]
29. Luo, H.; Dong, H.; Huang, M. Effect of intercritical annealing on the Lüders strains of medium Mn transformation-induced plasticity steels. *Mater. Des.* **2015**, *83*, 42–48. [[CrossRef](#)]
30. Han, J.; Lee, S.; Jung, J.; Lee, Y. The effects of the initial martensite microstructure on the microstructure and tensile properties of intercritically annealed Fe-9Mn-0.05C steel. *Acta Mater.* **2014**, *78*, 369–377. [[CrossRef](#)]
31. Li, Z.; Ding, H.; Misra, R.; Cai, Z. Deformation behavior in cold-rolled medium-manganese TRIP steel and effect of pre-strain on the Lüders bands. *Mater. Sci. Eng. A* **2017**, *679*, 230–239. [[CrossRef](#)]
32. Luo, H.; Liu, J.; Dong, H. A Novel Observation on Cementite Formed During Intercritical Annealing of Medium Mn Steel. *Metall. Mater. Trans. A* **2016**, *47*, 3119–3124. [[CrossRef](#)]
33. Lee, S.; Lee, S.; De Cooman, B. Constitutive Modeling of the Mechanical Properties of V-added Medium Manganese TRIP Steel. *Metall. Mater. Trans. A* **2013**, *44*, 3136–3146. [[CrossRef](#)]
34. Lee, C.; Jeong, J.; Han, J.; Lee, S.; Lee, S.; Lee, Y. Coupled strengthening in a medium manganese lightweight steel with an in-homogeneously grained structure of austenite. *Acta Mater.* **2015**, *84*, 1–8. [[CrossRef](#)]
35. Jimenez-Melero, E.; Dijk, N.; Zhao, L.; Sietama, J.; Zwaag, S. Martensitic transformation of individual grains in low-alloyed TRIP steels. *Scr. Mater.* **2007**, *56*, 421–424. [[CrossRef](#)]
36. Yang, D.; Du, P.; Wu, D.; Yi, H. The microstructure evolution and tensile properties of medium-Mn steel heat-treated by a two-step annealing process. *J. Mater. Sci. Technol.* **2021**, *75*, 205–215. [[CrossRef](#)]

Disclaimer/Publisher’s Note: The statements, opinions and data contained in all publications are solely those of the individual author(s) and contributor(s) and not of MDPI and/or the editor(s). MDPI and/or the editor(s) disclaim responsibility for any injury to people or property resulting from any ideas, methods, instructions or products referred to in the content.